

Supplementary Information

Hard X-ray-based techniques for structural investigations of CO₂ methanation catalysts prepared by MOF decomposition

Nils Prinz,^{a,#} Leif Schwensow,^{b,#} Sven Wendholt,^{c,#} Andreas Jentys^d, Matthias Bauer,^{c,*} Wolfgang Kleist^{b,*} and Mirijam Zobel^{a,*}

^a Chemistry Department, University Bayreuth, Universitätsstr. 30, Bayreuth 95447, Germany

^b Faculty of Chemistry and Biochemistry, Ruhr University Bochum, Universitätsstr. 150, 44801 Bochum

^c Chemistry Department, Paderborn University, Warburger Str. 100, Paderborn 33098, Germany

^d Department of Chemistry, Technical University of Munich, Lichtenbergstr. 4, 85748 Garching

[#]Contributed equally to this work.

Table of contents

General methods and approaches	2
XAS analysis	2
PDF refinement procedures	2
Radial distribution function and coordination numbers from PDF data	3
Determination of conversion and selectivity using gas chromatography	4
Material characterization and analysis.....	5
Attenuated total reflection infrared spectroscopy (ATR-IR).....	5
¹ H nuclear magnetic resonance (NMR) spectroscopy	6
Ion coupled plasma optical emission spectroscopy (ICP-OES)	6
Specific surface areas from N ₂ physisorption	7
Powder X-ray diffraction (PXRD)	7
Particle size estimation with Scherrer equation.....	8
Williamson-Hall plots – evaluation of particle size and strain.....	9
XANES analysis.....	10
EXAFS analysis	11
X-ray total scattering analysis.....	15
Transmission electron microscopy	18
Particle size estimation via EXAFS analysis.....	20
Comparison of coordination numbers from EXAFS and RDF analysis	21
References.....	21

General methods and approaches

XAS analysis

The XANES analysis, the LC-XANES fitting and the data preparation have been carried out with the program Athena of the demeter program package¹. For data evaluation, the spectra background has to be removed in first instance and, therefore, a Victoreen-type polynomial was subtracted.¹⁻⁴ The first inflection point was taken as energy $E_{(0)}$. To determine the smooth part of the spectrum, a piecewise polynomial was used. It was adjusted in a way to minimize the low-R components of the resulting Fourier transform. Afterwards the background-subtracted spectrum was divided by its smoothed part and the photon energy was converted to photoelectron wave number k . For the detailed EXAFS analysis, the resulting functions were weighted with k^3 and calculated with EXCURVE98, which works based on the EXAFS function and according to a formulation in terms of radial distribution functions.^{4,5}

$$\chi(k) = \sum_j S_0^2(K) F_j(k) \int P_j(r_j) \frac{e^{-\frac{2r_j}{\lambda}}}{kr_j^2} \sin[2kr_j + \delta_j(k)] dr_j$$

The number of independent points N_{ind} was calculated according to information theory to determine the degree of overdeterminacy:⁵

$$N_{ind} = \frac{2\Delta k \Delta R}{\pi}$$

In this formula, Δk describes the range in k -space used for the data analysis and in ΔR the corresponding radial distance range in the Fourier filtering process is observable. For Δk the area from 3 to 14 in k -space has been used for analysis, leading to Δk of 11. In the R -space 1 to 6 was used, leading to ΔR of 5. So the number of independent parameters is 35, according to the given equation.

For the determination of the quality of the fit, two methods were used. The reduced χ^2_{red} considers the degree of overdeterminacy of the system and the number of fitted parameters p . Leading to the possibility to compare different models directly:⁶

$$\chi^2_{red} = \frac{\left(\frac{N_{ind}}{N}\right)}{N_{ind} - p} \sum_i \left(\frac{k_i^n}{\sum_j k_j^n |\chi_j^{exp}(k_j)|} \right)^2 [\chi^{exp}(k_j) - \chi^{theo}(k_j)]^2$$

With the R-factor, the percentage disagreement between experiment and adjusted function is shown. Thereby, it considers both systematic and random errors.⁶

$$R = \sum_i \frac{k_i^n}{\sum_j k_j^n |\chi_j^{exp}(k_j)|} |\chi^{exp}(k_j) - \chi^{theo}(k_j)| \cdot 100\%$$

PDF refinement procedures

The refinements were done with *DiffPy-CMI*, a python-based complex modelling software.¹⁰ A Ni fcc crystallographic information file was used as the theoretical model for single-phase fits, and NiO and Ni hcp structures were used additionally for multi-phase fits. During the least squares refinements, we refined the lattice parameters a for the cubic, respectively a and c for the hexagonal structure, the atomic thermal motion parameter B_{isoj} , correlated motion of nearest neighbors δ_2 ¹¹, the spherical crystallite diameter (based on an isotropic attenuated crystal model) and a scale factor. The goodness of fit is described by the least square residuum R_w :

$$R_w = \sqrt{\frac{\sum_n (G_{obs,n} - G_{calc,n})^2}{\sum_n G_{obs,n}^2}}$$

Radial distribution function and coordination numbers from PDF data

The radial distribution function (RDF) $R(r)$ can be derived from the pair distribution function $G(r)$.

$$R(r) = [G(r) + 4\pi\rho_0r]r$$

The average number density ρ_0 is empirically extracted from the negative linear slope of the low r region in the PDF.⁸ The coordination number N_C is defined as the number of atoms between distance

$$N_C = \int_{r_1}^{r_2} R(r) dr$$

r_1 and r_2 ($r_1 < r_2$), i.e. .⁹ The integral of the peaks in the properly normalized $R(r)$ yields the coordination number.

Although the PDF is not normalized on an absolute scale, the ratio of the coordination numbers is maintained by the ratio of peak areas. They can thus be normalized with the XAS coordination numbers. For this we set the N_C of the 1st peak equal to the EXAFS analysis and apply the necessary scaling factor to the other N_C .

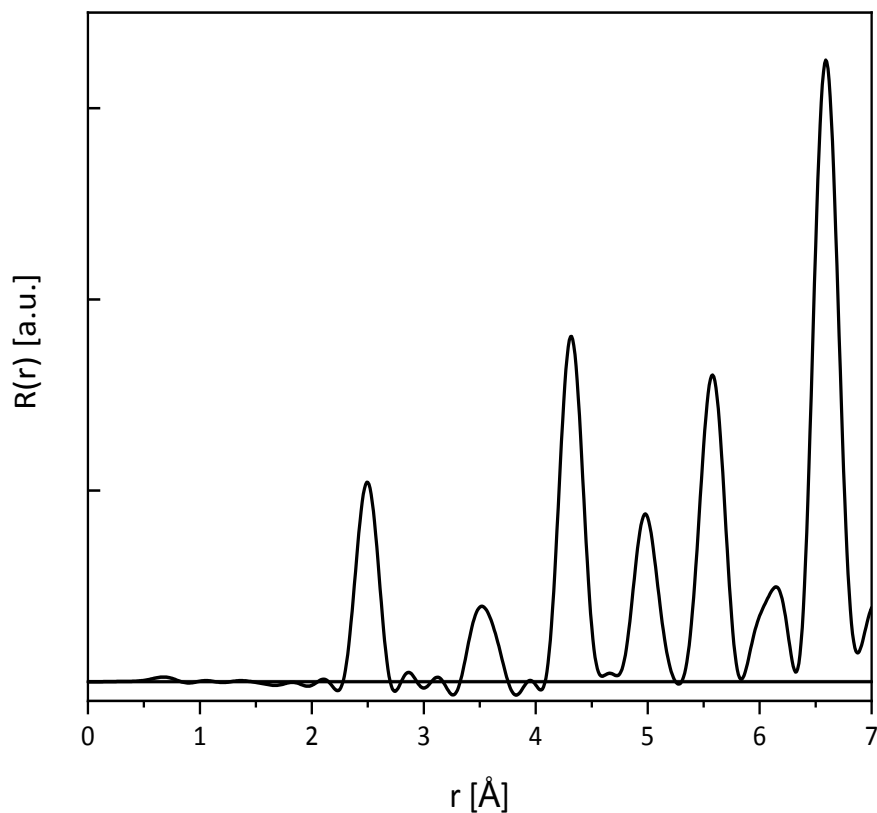


Fig.S1 Radial distribution function of Ni(BDC)(PNO) decomposed at 500 °C in 10% H₂/He.

Determination of conversion and selectivity using gas chromatography

The conversions of the methanation reaction were calculated using the following equation:

$$\text{conversion: } X(\text{CO}_2) = \left(1 - \frac{\text{CO}_{2,\text{out}}}{\text{CO}_{2,\text{out}} + \text{CO}_{\text{out}} + \text{CH}_{4,\text{out}} + \text{C}_2\text{H}_{6,\text{out}}} \right) \cdot 100\%$$

For conversions above 10%, Ar was used as an internal standard to correct for reaction-related volume contractions:

$$\text{conversion: } X'(\text{CO}_2) = \left(1 - \frac{\text{CO}_{2,\text{out}} \cdot \text{Ar}_{\text{in}}}{\text{CO}_{2,\text{in}} + \text{Ar}_{\text{out}}} \right) \cdot 100\%$$

The yields and selectivities were determined according to the following equations:

$$\text{yield: } Y(\text{CH}_4) = \left(\frac{\text{CH}_{4,\text{out}} \cdot \text{Ar}_{\text{in}}}{\text{CO}_{2,\text{in}} \cdot \text{Ar}_{\text{out}}} \right) \cdot 100\%$$

$$\text{yield: } Y(\text{CO}) = \left(\frac{\text{CO}_{\text{out}} \cdot \text{Ar}_{\text{in}}}{\text{CO}_{2,\text{in}} \cdot \text{Ar}_{\text{out}}} \right) \cdot 100\%$$

$$\text{selectivity: } S(\text{CH}_4) = \frac{Y(\text{CH}_4)}{X(\text{CO}_2)} \cdot 100\%$$

$$\text{selectivity: } S(\text{CO}) = \frac{Y(\text{CO})}{X(\text{CO}_2)} \cdot 100\%$$

Material characterization and analysis

Samples were characterized using various methods including attenuated total reflectance infrared (ATR-IR) spectroscopy, ^1H nuclear magnetic resonance (NMR) spectroscopy, N_2 physisorption analysis, ion coupled plasma optical emission (ICP-OES) spectroscopy, powder X-ray diffraction (PXRD), X-ray absorption spectroscopy (XAS), pair distribution function (PDF) and transmission electron microscopy (TEM).

Attenuated total reflection infrared spectroscopy (ATR-IR)

ATR-IR spectroscopy was performed using undiluted powder samples at room temperature at a Nicolet 6799 FT-IR spectrometer with a Smart iTX Diamant-ATR detector from Thermo Fisher Scientific. The final spectrum was calculated by the mean of 100 scans for wavenumbers between 400 cm^{-1} and 4000 cm^{-1} with a resolution of 4 cm^{-1} .

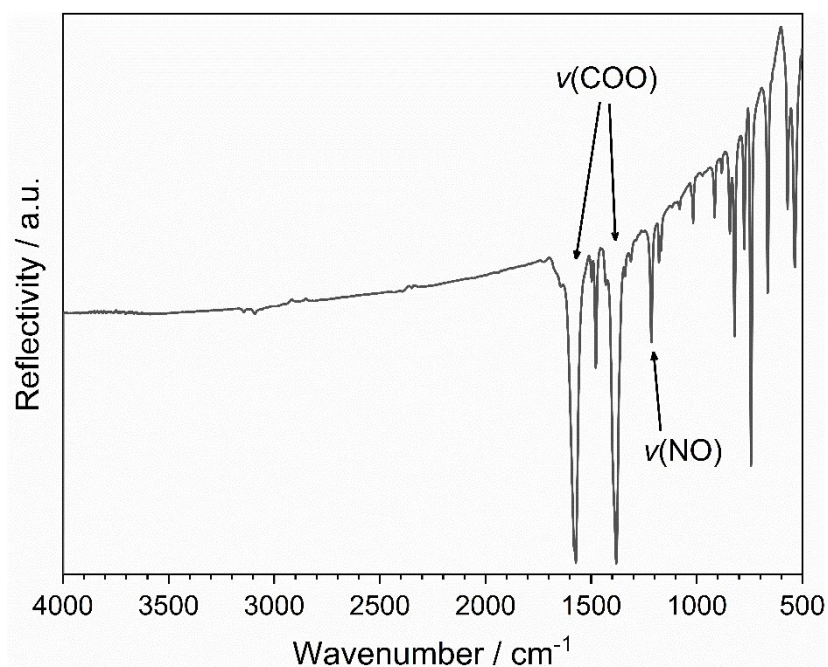


Fig. S2 ATR-IR spectrum of Ni(BDC)(PNO).

¹H nuclear magnetic resonance (NMR) spectroscopy

For ¹H-NMR spectroscopy, approximately 5 mg of MOF material was mixed with 70 μ L DCl/D₂O and treated for 3 min in an ultrasonic bath. Subsequently, 140 μ L NaOD/D₂O and 150 D₂O were added and placed in an ultrasonic bath for several minutes. The suspension was centrifuged at 10,000 min⁻¹ and the liquid was transferred into a NMR tube. The residual solid was mixed with 50 μ L NaOD/D₂O and 150 μ L D₂O. After treatment in an ultrasonic bath and centrifugation, this liquid was added to the same NMR tube. The liquid phase ¹H NMR spectrum was recorded with a Bruker Ascend 400 MHz spectrometer and referenced to tetramethylsilane.

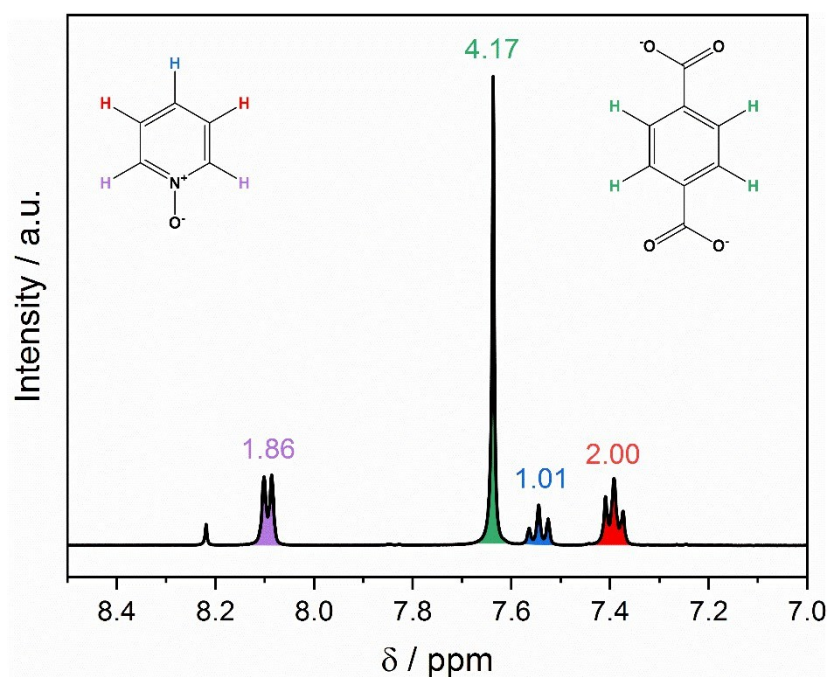


Fig. S3 ¹H nuclear magnetic resonance (NMR) spectrum of Ni(BDC)(PNO).

Ion coupled plasma optical emission spectroscopy (ICP-OES)

Prior to the ICP-OES analysis, 4-15 mg of the sample were burned in a crucible over a Bunsen burner. HCl was added and evaporated to form NiCl₂. Subsequently, the sample was dissolved in HNO₃ and transferred to a volumetric flask that was then filled with deionized water. Inductively coupled plasma optical emission spectroscopy (ICP-OES) of the solutions was performed with an iCAP 6500 Duo from Thermo Scientific via a six-point calibration. The software iTEVA9.8 was used for data processing.

Table S1 ICP-OES results for all decomposed samples.

Decomposition temperature	Ni content according to ICP-OES / wt%		
	0% H ₂ /He	5% H ₂ /He	10% H ₂ /He
350 °C	23	26	27
375 °C	35	60	61
400 °C	42	66	68
500 °C	53	72	82

Specific surface areas from N₂ physisorption

Specific surface areas were determined from nitrogen physisorption measurements using the BET method. The samples were dried for 20 h at 130 °C under vacuum and the measurements were performed with an Autosorb 6 setup from Quantachrome.

Table S2 BET surface analysis of all decomposed samples.

Decomposition temperature	Specific surface area according to BET / m ² /g		
	0% H ₂ /He	5%H ₂ /He	10%H ₂ /He
350 °C	5	48	44
375 °C	32	102	111
400 °C	23	56	77
500 °C	127	89	63

Powder X-ray diffraction (PXRD)

Powder X-ray diffraction was carried out at room temperature with a STOE STADI P Mythen2 4K diffractometer (Ge(111) monochromator; Ag K α 1 radiation, $\lambda = 0.5594 \text{ \AA}$) using four Dectris MYTHEN2 R 1K detector in Debye–Scherrer geometry. Samples were measured in 1 mm diameter Kapton capillaries for 12 h. The Q-range was 20.4 \AA^{-1} .

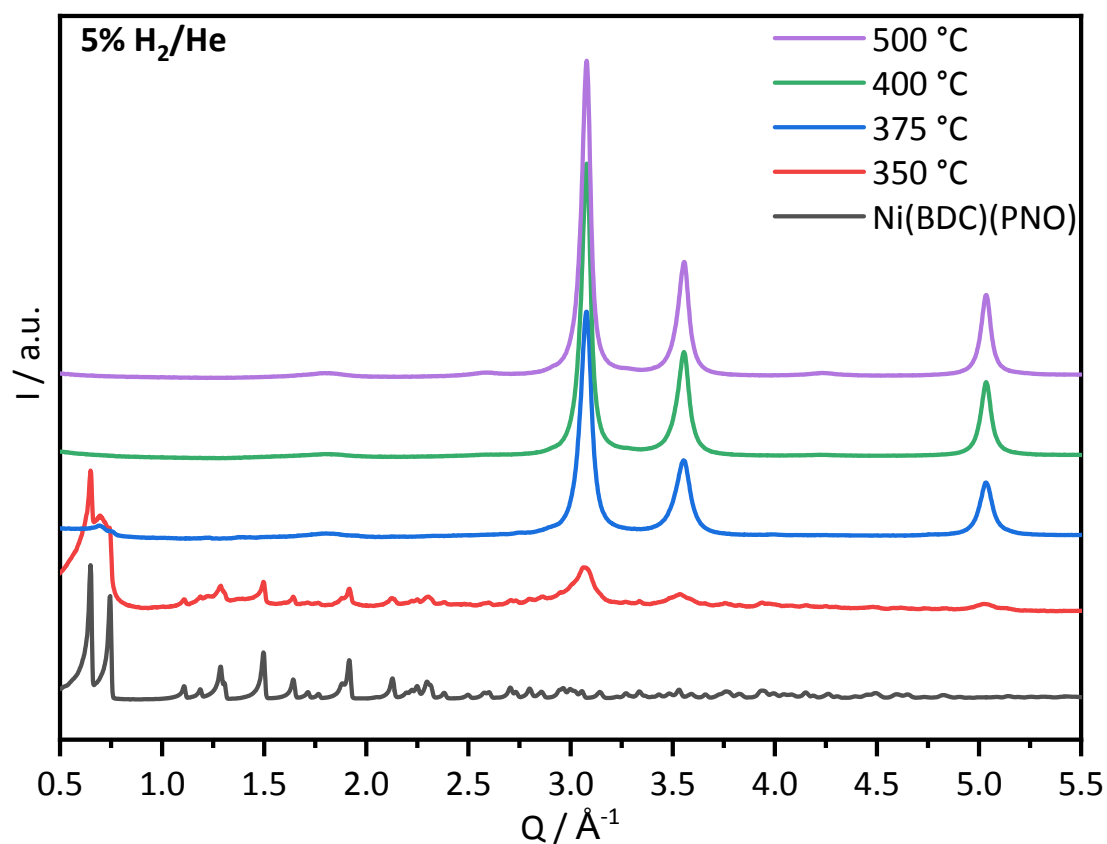


Fig. S4 PXRD of Ni(BDC)(PNO) decomposed at different temperatures in 5% H₂/He.

Particle size estimation with Scherrer equation

The Scherrer equation with the wave impulse vector Q was used to determine crystallite sizes:

$$D = \frac{K \cdot 2\pi}{FWHM(Q)}$$

$K = 0.89$ (*spherical shape constant*)

The first three Bragg reflections of Ni fcc (111), (200) and (220) were used for a single peak fit with a pseudo Voigt function from which the FWHM was extracted.

Table S3: Particle sizes using Scherrer equation for different reflections.

Decomposition temperature	Reflection (hkl)	Particle size after decomposition in different atmospheres / nm		
		0% H ₂ /He	5% H ₂ /He	10% H ₂ /He
350 °C	(111)	-	6.0	7.2
	(200)	-	5.9	5.4
	(220)	-	4.5	7.0
375 °C	(111)	7.1	12.2	13.6
	(200)	3.0	8.2	9.6
	(220)	-	10.4	11.7
400 °C	(111)	11.5	15.8	14.6
	(200)	8.3	11.1	10.4
	(220)	11.3	13.6	12.9
500 °C	(111)	12.9	16.7	24.2
	(200)	8.6	12.1	19.7
	(220)	12.1	14.6	21.5

Williamson-Hall plots – evaluation of particle size and strain

XRD data was further analyzed with Williamson-Hall plots to separate particle size broadening from strain-induced broadening. The following equations provide the correlation of full width half maxima FWHM, scattering angle 2ϑ , Scherrer constant K (0.89 for spherical shape), employed wavelength λ (0.059 nm), particle diameter D and strain ε . For a plot of FWHM vs. $\sin(\vartheta)$, particle size can thus be evaluated from the y-axis intercept and strain induced broadening from the slope of a straight line, if all data points (FWHM of all hkl reflexes) fall onto this line. The individual peak positions and FWHM have been determined from single peak fits using a pseudo-Voigt function. Instrumental broadening was accounted for with a LaB_6 standard measurement, by plotting the instrumental broadening FWHM_{ins} against peak position 2ϑ . A 2nd order polynomial function was used to fit this instrumental broadening.

$$\text{FWHM} * \cos(\theta) = \frac{K * \lambda}{D} + 4 * \sin(\theta) * \varepsilon$$

$$D = \frac{K * \lambda}{y - \text{intercept}}$$

$$\varepsilon = \text{slope}$$

FWHM of all hkl reflections, except 200 and 400, fall onto a line for all samples, as shown for the 375 °C in 5 % H_2/He sample in Fig. S5. The following table provides the derived particle diameters and strain for all samples. As can be seen in Fig. S5, strain is homogeneous in different crystallographic directions of the particle, since the two straight lines in Fig. S5 have the same slope. However, particle size in the 200 direction is smaller (which was already estimated from Debye Scherrer neglecting ostrain broadening).

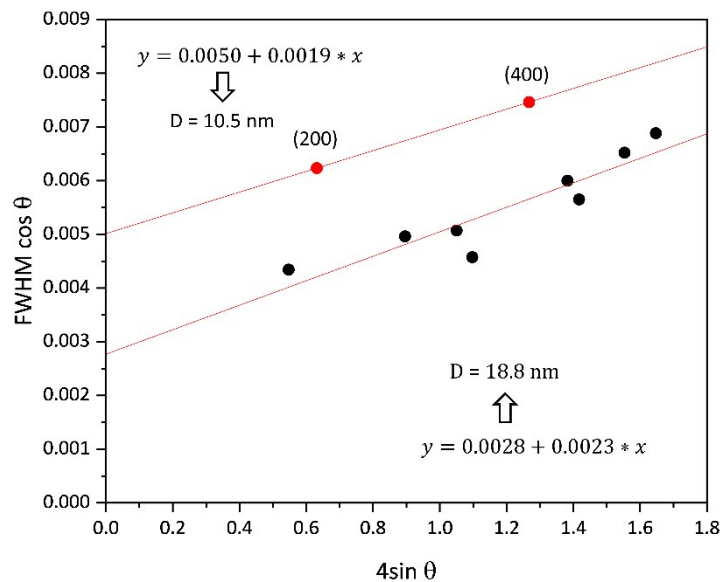


Fig. S5 Williamson-Hall plot of the sample decomposed at 375 °C in 5% H_2/He (catalytically most active sample). The red dots for the (200) and (400) reflection were not taken into account for the linear fit through the black data points.

Table S4: Particle sizes and strain extracted from Williamson-Hall plots. Different lower and upper error margins result for the particle diameters from the x^{-1} dependency of the diameter from the y-axis intercept, as shown in brackets.

Particle size / nm			
Temperature	0 % H ₂ /He	5% H ₂ /He	10% H ₂ /He
375	- ^a	18.8 (+4.1 / -2.8)	17.5 (+1.9 / -1.6)
400	15.9 (+4.6 / -2.8)	15.9 (+1.6 / -1.3)	18.8 (+2.3 / -1.8)
500	15.0 (+1.4 / -1.2)	21.9 (+3.1 / -2.4)	20.2 (+0.8 / -0.7)
Strain ϵ corresponding to $\Delta d/d$			
375	- ^a	0.0023 \pm 0.0004	0.0016 \pm 0.0003
400	0.0016 \pm 0.0005	0.0018 \pm 0.0002	0.0013 \pm 0.0003
500	0.0011 \pm 0.0002	0.0013 \pm 0.0002	0.0012 \pm 0.0001

^a For 350 °C 0/5/10% H₂/He and 375 °C 0% H₂/He overlaps with phases that differs from fcc Ni were present. An accurate calculation of FWHM of a statistical amount of peaks was not possible.

XANES analysis

Table S5 Linear Combination fitting of the XANES spectra. Ni foil and Ni(BDC)(PNO) have been used as references for Ni⁰ and Ni^{II}, respectively.

Sample	Fraction Ni ⁰ / %	Fraction Ni ^{II} / %	Fraction Ni ⁰ (floating E ₀) / %	Fraction Ni ^{II} (floating E ₀) / %
Ni@C-0%H ₂ -350	19.2 \pm 0.8	80.8 \pm 0.8	18.6 \pm 0.6	81.4 \pm 0.6
Ni@C-0%H ₂ -375	62.3 \pm 0.6	37.7 \pm 0.6	62.4 \pm 0.6	37.6 \pm 0.6
Ni@C-0%H ₂ -400	83.0 \pm 0.7	17.0 \pm 0.7	82.7 \pm 0.7	17.3 \pm 0.7
Ni@C-0%H ₂ -500	95.1 \pm 3.0	4.9 \pm 3.0	90.5 \pm 2.3	9.5 \pm 2.3
Ni@C-5%H ₂ -350	31.1 \pm 1.0	68.9 \pm 1.0	30.4 \pm 0.5	69.6 \pm 0.5
Ni@C-5%H ₂ -375	88.2 \pm 0.3	11.8 \pm 0.3	88.1 \pm 0.3	11.9 \pm 0.3
Ni@C-5%H ₂ -400	92.4 \pm 1.2	7.6 \pm 1.2	91.2 \pm 0.9	8.8 \pm 0.9
Ni@C-5%H ₂ -500	95.4 \pm 1.6	4.6 \pm 1.6	93.8 \pm 1.3	6.2 \pm 1.3
Ni@C-10%H ₂ -350	36.0 \pm 0.8	64.0 \pm 0.8	35.6 \pm 0.4	64.4 \pm 0.4
Ni@C-10%H ₂ -375	85.7 \pm 0.5	14.3 \pm 0.5	85.4 \pm 0.4	14.6 \pm 0.4
Ni@C-10%H ₂ -400	88.2 \pm 0.8	11.8 \pm 0.8	87.7 \pm 0.6	12.3 \pm 0.6
Ni@C-10%H ₂ -500	92.9 \pm 1.6	7.1 \pm 1.6	91.4 \pm 1.3	8.6 \pm 1.3

EXAFS analysis

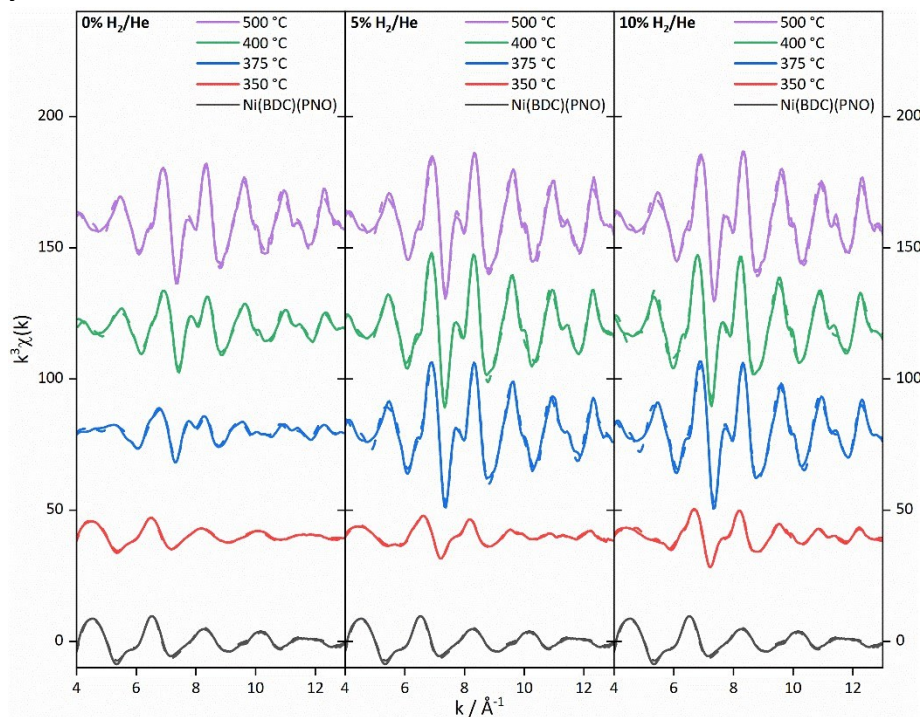


Fig. S6 Experimental $k^3\chi(k)$ EXAFS function of the MOF precursor decomposed in 0% (left), 5% hydrogen (middle) and 10% hydrogen in helium (right) atmosphere. The solid line shows the experimental spectra, the dotted line shows the theoretical fit of the EXAFS analysis.

Table S6 Structural parameter obtained by fitting the experimental EXAFS spectra of the sample, which have been decomposed in 0% H₂/He atmosphere in comparison to the catalyst precursor.

Sample	Abs-Bs ^a	N(Bs) ^b	R(Abs-Bs) ^c /Å	σ^d /Å ⁻¹	R ^e /%, χ_{red}^{2f} , E _f ^g /eV, A _{fac} ^h
Ni(BDC)(PNO)	Ni – O	6.1 ± 0.3	2.04 ± 0.02	0.084 ± 0.008	16.13
	Ni – C	6.6 ± 0.7	2.97 ± 0.03	0.110 ± 0.001	2.10 × 10 ⁻⁶
	Ni – Ni	1.4 ± 0.3	3.52 ± 0.04	0.089 ± 0.009	7.243
	Ni – C	5.3 ± 1.1	3.98 ± 0.04	0.102 ± 0.010	1.048
	Ni – C	10.7 ± 2.2	4.49 ± 0.04	0.112 ± 0.011	
Ni@C-0%H ₂ -350	Ni – O	6.8 ± 0.4	2.05 ± 0.02	0.092 ± 0.009	16.82
	Ni – C	7.2 ± 1.4	3.02 ± 0.03	0.112 ± 0.011	1.74 × 10 ⁻⁶
	Ni – Ni	1.1 ± 0.2	3.52 ± 0.04	0.112 ± 0.011	5.549
	Ni – C	6.6 ± 1.3	3.97 ± 0.04	0.110 ± 0.011	0.8000
	Ni – O	4.8 ± 1.0	4.44 ± 0.04	0.112 ± 0.011	
Ni@C-0%H ₂ -375	Ni – O	2.8 ± 0.3	1.99 ± 0.02	0.110 ± 0.011	35.00
	Ni – Ni	3.5 ± 0.4	2.50 ± 0.03	0.095 ± 0.010	7.6 × 10 ⁻⁶
	Ni – C	2.4 ± 0.2	2.98 ± 0.03	0.032 ± 0.003	10.71
	Ni – Ni	1.6 ± 0.3	3.47 ± 0.03	0.110 ± 0.011	0.8581
	Ni – C	3.7 ± 0.7	3.85 ± 0.04	0.039 ± 0.004	
	Ni – Ni	3.4 ± 0.7	4.28 ± 0.04	0.087 ± 0.009	
	Ni – Ni	6.6 ± 1.3	5.10 ± 0.05	0.097 ± 0.010	
Ni@C-0%H ₂ -400	Ni – Ni	6.9 ± 0.7	2.49 ± 0.03	0.095 ± 0.010	22.74
	Ni – Ni	2.4 ± 0.5	3.41 ± 0.03	0.112 ± 0.011	2.67 × 10 ⁻⁶
	Ni – C	3.7 ± 0.7	3.82 ± 0.04	0.022 ± 0.002	16.45
	Ni – Ni	7.4 ± 1.5	4.24 ± 0.04	0.095 ± 0.010	0.8148
	Ni – Ni	10.2 ± 2.1	5.06 ± 0.05	0.089 ± 0.009	
Ni@C-0%H ₂ -500	Ni – Ni	8.1 ± 0.8	2.47 ± 0.02	0.081 ± 0.008	21.46
	Ni – Ni	3.8 ± 0.8	3.49 ± 0.03	0.112 ± 0.011	3.03 × 10 ⁻⁶
	Ni – C	3.8 ± 0.8	3.80 ± 0.04	0.032 ± 0.003	0.1029
	Ni – Ni	17.0 ± 3.4	4.28 ± 0.04	0.102 ± 0.010	0.8000
	Ni – Ni	19.6 ± 3.9	5.10 ± 0.05	0.095 ± 0.010	

^a Abs: X-ray absorbing atom, and Bs: backscattering atom. ^b Number of backscattering atoms. ^c Distance of the absorbing atom from the backscattering atom. ^d Debye-Waller like factor. ^e Fit index. ^f Reduced χ^2 . ^g Fermi energy, which accounts for the shift between theory and experiment. ^h Amplitude reduction factor.

Table S7 Structural parameter obtained by fitting the experimental EXAFS spectra of the sample, which have been decomposed in 5% H₂/He atmosphere in comparison to the catalyst precursor.

Sample	Abs-Bs ^a	N(Bs) ^b	R(Abs-Bs) ^c /Å	σ^d /Å ⁻¹	R ^e /%, χ_{red}^{2f} , E _F ^g /eV, A _{fac} ^h
Ni(BDC)(PNO)	Ni – O	6.1 ± 0.3	2.04 ± 0.02	0.084 ± 0.008	16.13
	Ni – C	6.6 ± 0.7	2.97 ± 0.03	0.110 ± 0.001	2.10 × 10 ⁻⁶
	Ni – Ni	1.4 ± 0.3	3.52 ± 0.04	0.089 ± 0.009	7.243
	Ni – C	5.3 ± 1.1	3.98 ± 0.04	0.102 ± 0.010	1.048
	Ni – C	10.7 ± 2.2	4.49 ± 0.04	0.112 ± 0.011	
Ni@C-5%H ₂ -350	Ni – O	5.5 ± 0.6	2.05 ± 0.02	0.092 ± 0.009	16.21
	Ni – Ni	2.7 ± 0.3	2.51 ± 0.03	0.100 ± 0.010	2.95 × 10 ⁻⁶
	Ni – C	1.9 ± 0.4	3.05 ± 0.03	0.039 ± 0.004	4.932
	Ni – Ni	0.3 ± 0.0	3.50 ± 0.04	0.039 ± 0.004	0.8000
	Ni – C	5.9 ± 1.2	3.97 ± 0.04	0.74 ± 0.007	
	Ni – Ni	2.4 ± 0.5	4.35 ± 0.04	0.100 ± 0.010	
	Ni – Ni	4.3 ± 0.8	5.18 ± 0.05	0.105 ± 0.011	
Ni@C-5%H ₂ -375	Ni – Ni	11.8 ± 1.2	2.47 ± 0.02	0.084 ± 0.008	23.68
	Ni – Ni	4.2 ± 0.8	3.45 ± 0.03	0.112 ± 0.011	2.29 × 10 ⁻⁶
	Ni – C	6.7 ± 1.3	3.82 ± 0.04	0.045 ± 0.004	0.7178
	Ni – Ni	24.1 ± 4.8	4.28 ± 0.04	0.105 ± 0.011	12.89
	Ni – Ni	31.8 ± 6.2	5.10 ± 0.05	0.102 ± 0.010	
Ni@C-5%H ₂ -400	Ni – Ni	12.0 ± 1.2	2.48 ± 0.02	0.087 ± 0.009	16.45
	Ni – Ni	2.1 ± 0.4	3.46 ± 0.03	0.077 ± 0.008	1.62 × 10 ⁻⁶
	Ni – C	5.8 ± 1.2	3.86 ± 0.04	0.032 ± 0.003	-0.0646
	Ni – Ni	12.8 ± 2.6	4.28 ± 0.04	0.084 ± 0.008	0.7353
	Ni – Ni	23.0 ± 4.6	4.76 ± 0.05	0.112 ± 0.011	
	Ni – Ni	35.6 ± 7.1	5.10 ± 0.05	0.112 ± 0.011	
Ni@C-5%H ₂ -500	Ni – Ni	10.5 ± 1.1	2.47 ± 0.02	0.081 ± 0.008	21.10
	Ni – Ni	3.6 ± 0.7	3.46 ± 0.03	0.100 ± 0.010	2.61 × 10 ⁻⁶
	Ni – C	4.0 ± 0.8	3.82 ± 0.04	0.032 ± 0.003	1.102
	Ni – Ni	19.9 ± 4.0	4.28 ± 0.04	0.095 ± 0.010	0.6908
	Ni – Ni	23.3 ± 4.7	5.09 ± 0.05	0.087 ± 0.009	
	Ni – Ni	3.1 ± 0.6	5.53 ± 0.06	0.045 ± 0.005	

^a Abs: X-ray absorbing atom, and Bs: backscattering atom. ^b Number of backscattering atoms. ^c Distance of the absorbing atom from the backscattering atom. ^d Debye-Waller like factor. ^e Fit index. ^f Reduced χ^2 . ^g Fermi energy, which accounts for the shift between theory and experiment. ^h Amplitude reduction factor.

Table S8 Structural parameter obtained by fitting the experimental EXAFS spectra of the sample, which have been decomposed in 10% H₂/He atmosphere in comparison to the catalyst precursor.

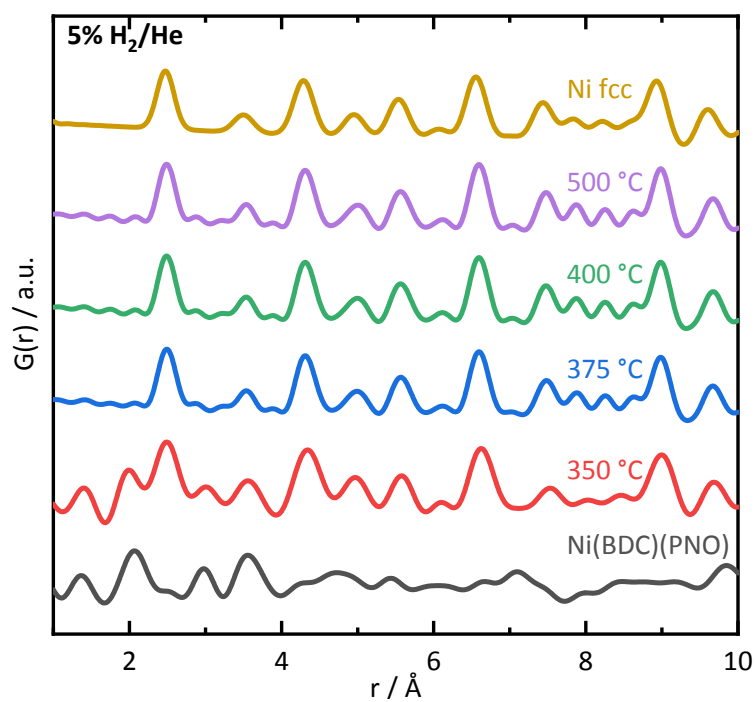
Sample	Abs-Bs ^a	N(Bs) ^b	R(Abs-Bs) ^c /Å	σ^d /Å ⁻¹	R ^e /%, χ_{red}^{2f} , E _f ^g /eV, A _{fac} ^h
Ni(BDC)(PNO)	Ni – O	6.1 ± 0.3	2.04 ± 0.02	0.084 ± 0.008	16.13
	Ni – C	6.6 ± 0.7	2.97 ± 0.03	0.110 ± 0.001	2.10 × 10 ⁻⁶
	Ni – Ni	1.4 ± 0.3	3.52 ± 0.04	0.089 ± 0.009	7.243
	Ni – C	5.3 ± 1.1	3.98 ± 0.04	0.102 ± 0.010	1.048ö
	Ni – C	10.5 ± 2.1	4.49 ± 0.04	0.112 ± 0.011	
Ni@C-10%H ₂ -350	Ni – O	5.6 ± 0.6	2.06 ± 0.02	0.097 ± 0.010	19.62
	Ni – Ni	3.5 ± 0.4	2.48 ± 0.03	0.089 ± 0.009	2.15 × 10 ⁻⁶
	Ni – Ni	1.9 ± 0.4	3.49 ± 0.03	0.112 ± 0.011	4.879
	Ni – C	7.9 ± 1.6	3.94 ± 0.04	0.097 ± 0.010	0.7921
	Ni – Ni	2.0 ± 0.4	4.31 ± 0.04	0.071 ± 0.007	
	Ni – Ni	6.7 ± 1.3	4.80 ± 0.05	0.097 ± 0.010	
Ni@C-10%H ₂ -375	Ni – Ni	11.3 ± 1.1	2.47 ± 0.03	0.087 ± 0.009	22.68
	Ni – Ni	4.5 ± 0.9	3.46 ± 0.04	0.112 ± 0.011	2.55 × 10 ⁻⁶
	Ni – C	3.6 ± 0.7	3.84 ± 0.04	0.032 ± 0.003	12.95
	Ni – Ni	15.6 ± 3.1	4.26 ± 0.04	0.095 ± 0.010	0.7665
	Ni – Ni	25.1 ± 5,1	5.10 ± 0.05	0.095 ± 0.010	
	Ni – Ni	1.8 ± 0.36	5.54 ± 0.055	0.032 ± 0.003	
Ni@C-10%H ₂ -400	Ni – Ni	11.5 ± 1.2	2.48 ± 0.03	0.081 ± 0.008	18.93
	Ni – Ni	6.4 ± 1.3	3.49 ± 0.04	0.107 ± 0.011	2.14 × 10 ⁻⁶
	Ni – C	4.9 ± 1.0	3.92 ± 0.04	0.045 ± 0.004	9.699
	Ni – Ni	17.2 ± 3.4	4.31 ± 0.04	0.087 ± 0.009	0.6490
	Ni – Ni	21.9 ± 4.4	4.78 ± 0.05	0.089 ± 0.009	
	Ni – Ni	21.2 ± 4.2	5.57 ± 0.06	0.112 ± 0.011	
Ni@C-10%H ₂ -500	Ni – Ni	11.4 ± 1.1	2.47 ± 0.02	0.077 ± 0.008	21.05
	Ni – Ni	5.1 ± 1.0	3.46 ± 0.03	0.110 ± 0.011	2.52 × 10 ⁻⁶
	Ni – C	5.9 ± 1.2	3.82 ± 0.04	0.032 ± 0.003	0.6036
	Ni – Ni	21.5 ± 4.3	4.28 ± 0.04	0.092 ± 0.009	0.6351
	Ni – Ni	26.1 ± 5.2	5.09 ± 0.05	0.087 ± 0.009	
	Ni – Ni	3.4 ± 0.7	5.54 ± 0.06	0.039 ± 0.004	

^a Abs: X-ray absorbing atom, and Bs: backscattering atom. ^b Number of backscattering atoms. ^c Distance of the absorbing atom from the backscattering atom. ^d Debye-Waller like factor. ^e Fit index. ^f Reduced χ^2 . ^g Fermi energy, which accounts for the shift between theory and experiment. ^h Amplitude reduction factor.

X-ray total scattering analysis

The following total scattering data was acquired on the laboratory diffractometer. All samples were measured in Kapton capillaries with a diameter of 1 mm for 12 h. The powder diffraction patterns were collected in a Q-range of $0.3 - 20.4 \text{ \AA}^{-1}$. PDF calculation was done with PDFgetX3⁸ and PDF modelling with diffpy-cmi.⁹

Fig. S7 PDF of Ni(BDC)(PNO) decomposed at different temperatures in 10% H₂/He. As reference a calculated Ni fcc structure of particles with 10 nm size in diameter is shown



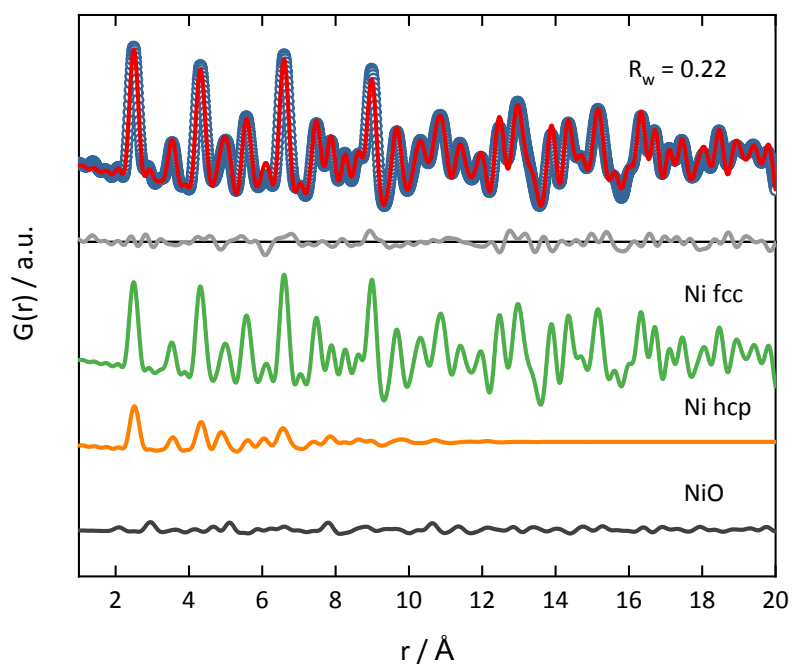


Fig. S8 PDF refinement of Ni(BDC)(PNO) decomposed at 400 °C in He. A small contribution of Ni hcp structure in the short range to the fit is still visible.

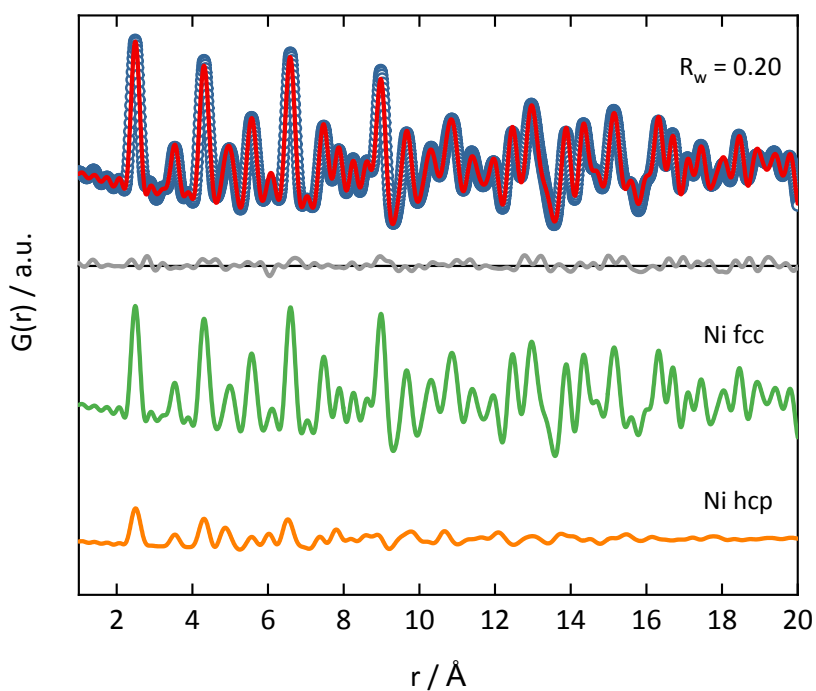


Fig. S9 PDF refinement of Ni(BDC)(PNO) decomposed at 500 °C in He. A small contribution of Ni hcp structure to the fit is still visible, but the overall ratio decreased from 375 °C to 500 °C.

For an overview of the robustness of the PDF modelling using Diffpy-CMI the refined values are exemplary showed for the sample decomposed at 375 °C in 0% H₂/He.

Table S9 Refined values from the Diffpy-CMI fit of the sample decomposed at 375 °C in 0% H₂/He.

Parameter	Refined value
B _{iso} Ni (fcc)	0.977 Å ²
B _{iso} Ni (hcp)	0.367 Å ²

B_{iso} Ni (NiO)	0.702 Å ²
B_{iso} O (NiO)	1.971 Å ²
a Ni fcc	4.17 Å
a NiO	3.53 Å
a Ni hcp	2.65 Å
c Ni hcp	4.34 Å
δ_2 Ni fcc	0.0
δ_2 Ni hcp	4.7
δ_2 NiO	6.9
Scale Ni fcc	0.30
Scale Ni hcp	0.15
Scale NiO	0.18
Particle size Ni fcc	48 Å
Particle size Ni hcp	55 Å
Particle size NiO	12 Å
R_w	0.32

Table S10 Change of the thermal displacement parameters U_{iso} extracted with Diffpy-CMI refinements

Temperature	U_{iso} 0%H ₂ /He	U_{iso} 5% H ₂ /He	U_{iso} 10%H ₂ /He
350°C	-	0.0121	0.0108
375°C	0.0124	0.0093	0.0086
400°C	0.0091	0.0084	0.0083
500°C	0.0081	0.0078	0.0083

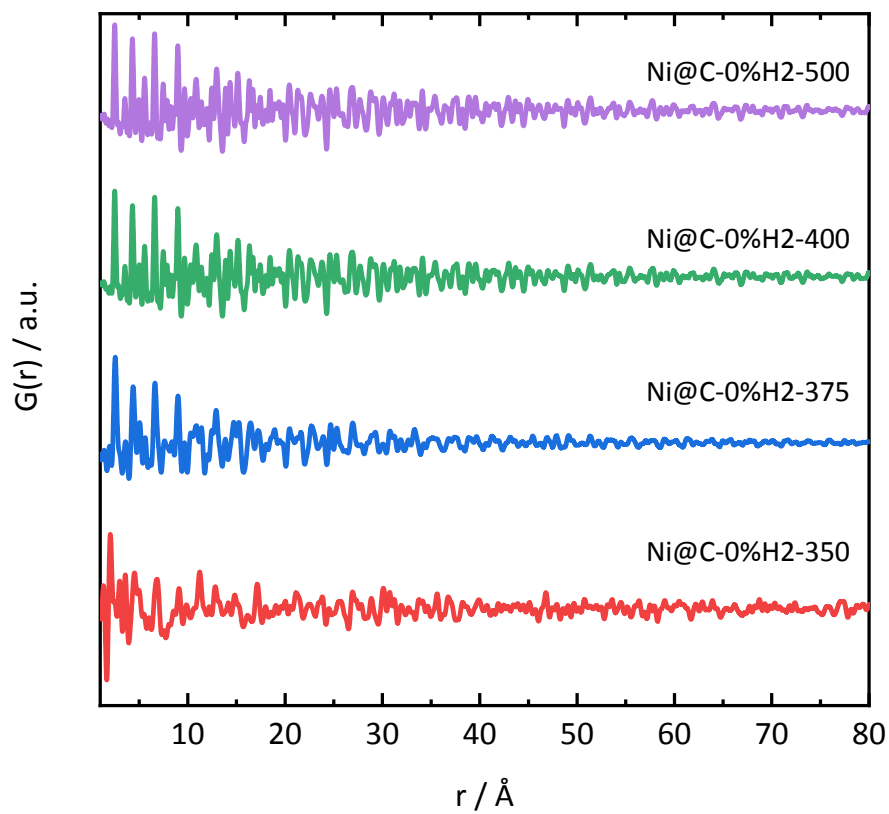


Fig. S10 PDF of Ni(BDC)(PNO) decomposed in 0% H₂/He over temperature in the range until 80 Å. The higher dampening in $G(r)$ for smaller crystalline domain sizes is clearly visible.

Transmission electron microscopy

Transmission electron microscopy images were collected using a JEOL JEM-2200FS equipped with Schottky field-emission gun operated at 200 kV and a magnetic in-column omega type energy filter. Images were acquired using a GatanOneView imaging filter with a CMOS camera. Samples were prepared by dipping a lacey carbon film coated on a copper grid (Electron Microscopy Sciences) into the sample powder. For determination of particle sizes, about 200 particles were counted for each sample. For most samples a lognormal distribution could be fitted to the histograms. To determine the anisotropy of particles, a comparison of the width and length of particles for the most active sample decomposed at 375 °C under 5% H₂/He was carried out. This comparison shows, that particle lengths on average exceed particle widths, i.e. leading to a small particle anisotropy with axes differing by ca. $(23.8-20.4)/23.8 = 14.3\%$.

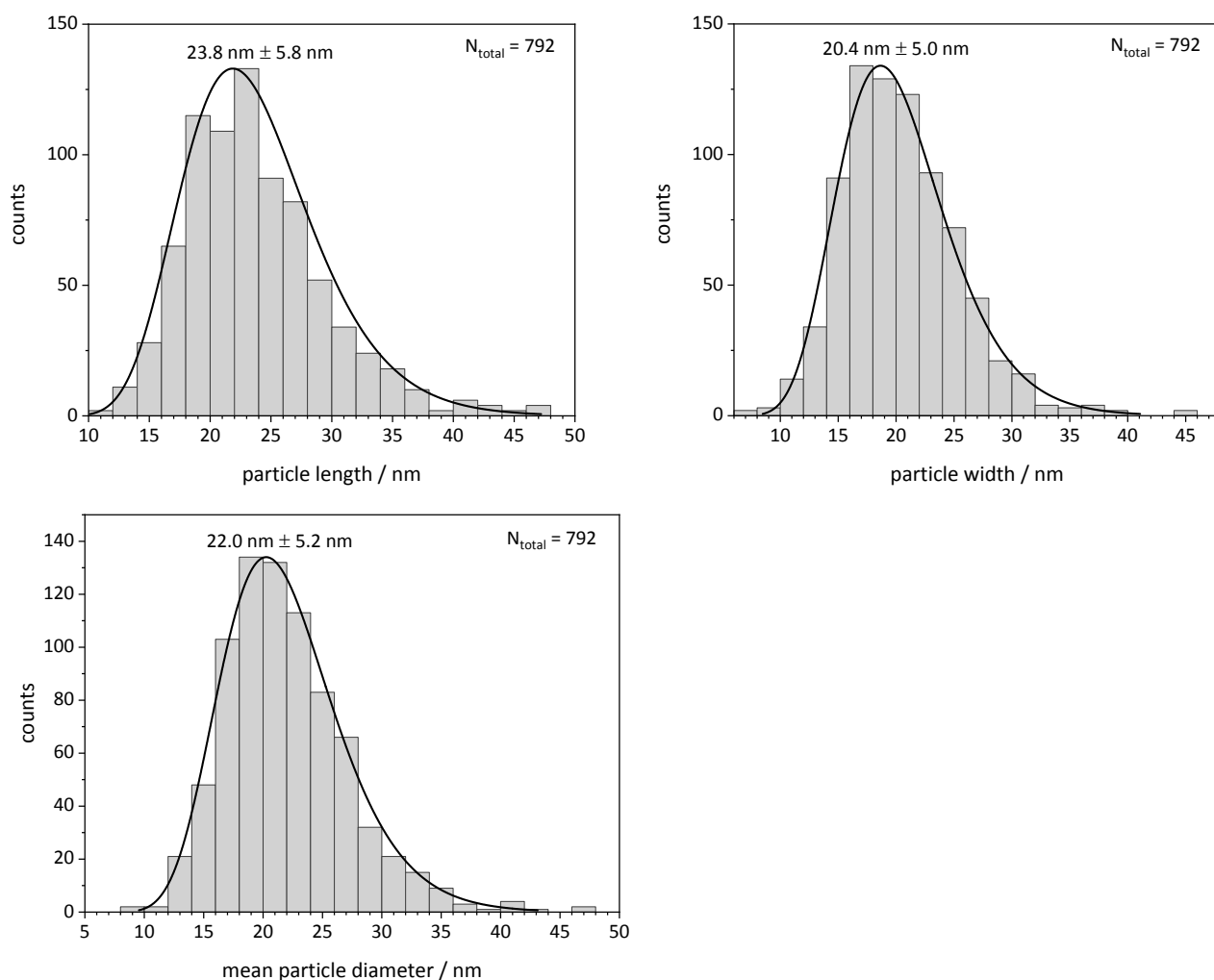


Fig. S11 Lognormal distributions for 375 °C 5% H₂/He using two orthogonal axes (length and width) for the particle sizes to investigate ellipsoidal contribution to the overall mean particle diameter. The lengths and widths are shown separately first (top row) and then averaged (bottom row).

TEM lognormal distributions 0% H₂/He

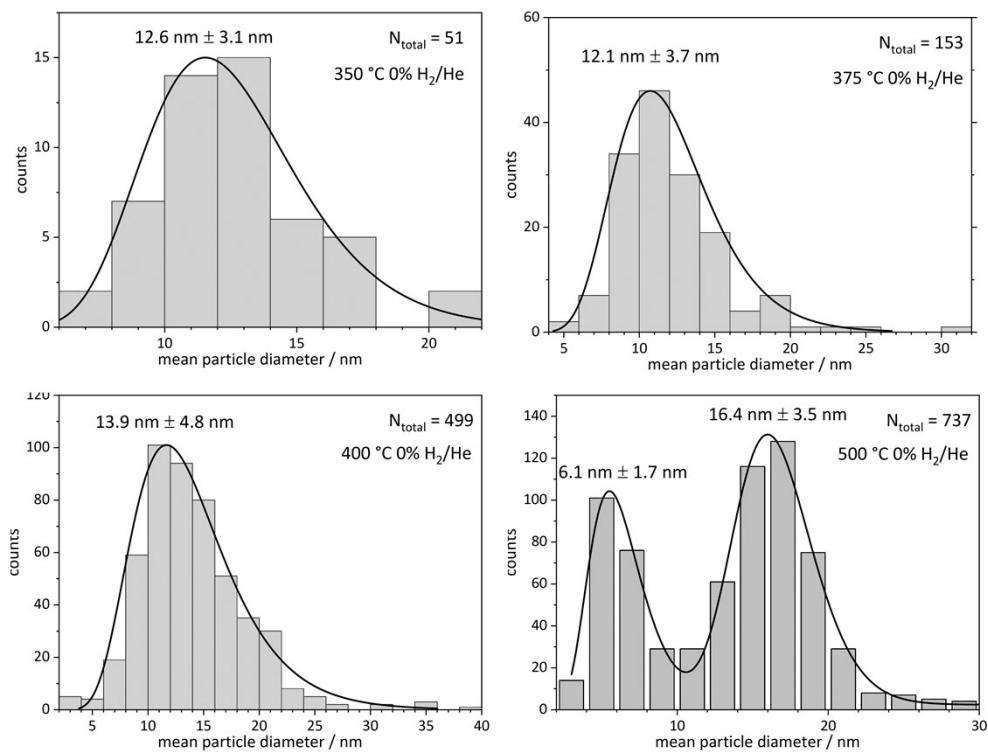


Fig. S12 Lognormal distribution of TEM particle sizes with mean diameter and standard deviation of the distribution for the samples decomposed under 0% H₂/He.

TEM lognormal distributions 10% H₂/He

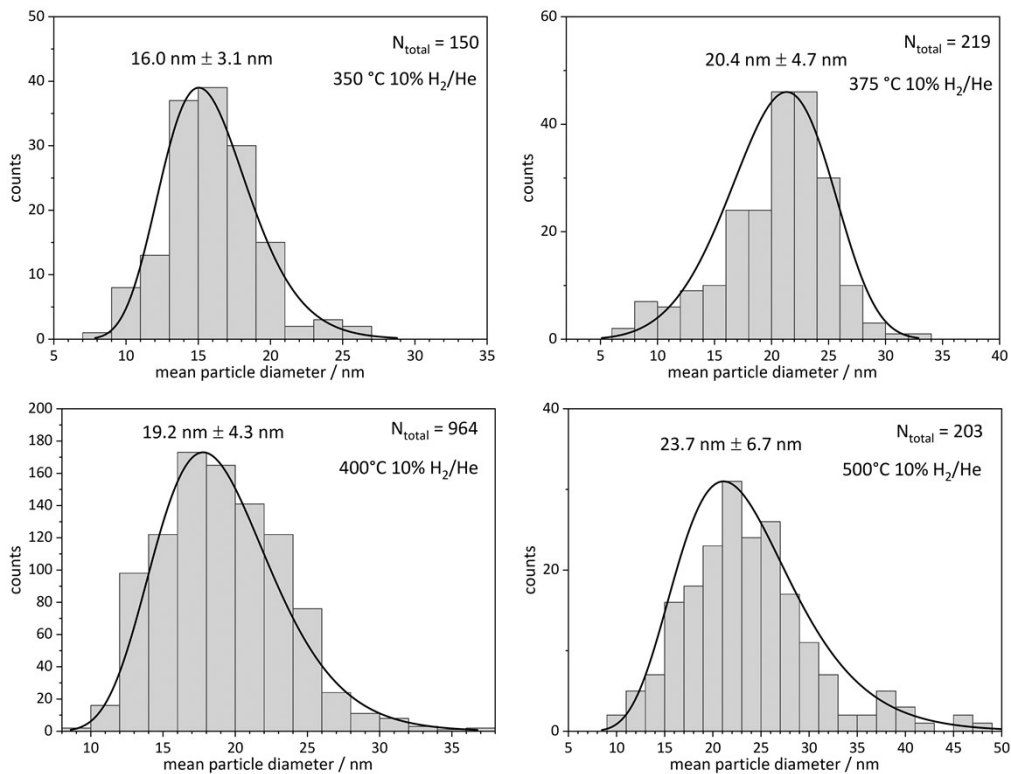


Fig. S13 Lognormal distribution (except 375 °C, which is a Weibull distribution) of TEM particle sizes with mean diameter and standard deviation of the distribution for the samples decomposed under 10% H₂/He.

Particle size estimation via EXAFS analysis

The method for particle size estimation is based on the following equation:⁷

$$N_i = \frac{aN_{at}}{b + N_{at}} + \frac{cN_{at}}{d + N_{at}}$$

N_i is the average number of neighbors in each coordination shell ($i=1-5$) as a function of atoms present in the cluster (N_{at}).⁷

Table S11: Parameters used to fit the coordination number (N_i) as a function of the number of atoms (N_{at}).

	N_1	N_2	N_3	N_4	N_5
a	8.981	3.922	13.204	6.830	10.609
b	9.640	7.368	39.134	55.369	37.582
c	3.026	2.192	11.593	5.684	14.265
d	1462.61	989.28	1292.24	1541.86	1020.82

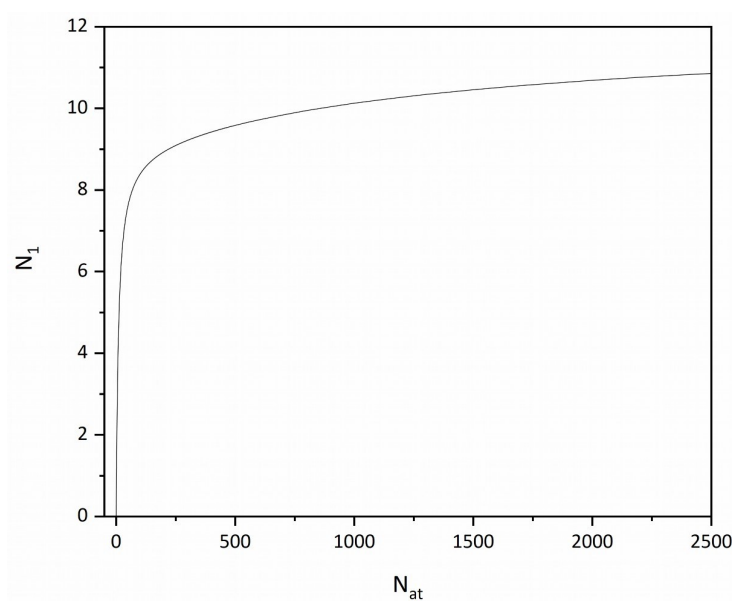


Fig. S14 Average coordination of the first coordination shell (N_1) as the number of atoms (N_{at}).

Comparison of coordination numbers from EXAFS and RDF analysis

Coordination numbers calculated from the radial distribution function derived from the experimental PDF are normalized with the 1st shell coordination number from EXAFS analysis. In contrast to EXAFS, coordination numbers beyond the third shell can be extracted, because of the smaller scattering and absorption cross sections and absence of multiple scattering of high energy X-rays compared to photoelectrons. The coordination numbers of the first three shells match well. The particle growth is also directly reflected in those increasing CN for distances beyond the XAS range, see for example at 6.6 Å.

Table S12 Coordination numbers from EXAFS and RDF analysis. Theoretical value for bulk Ni fcc in brackets.

Decomposition temperature	CN 1 st shell at 2.5 Å (theor. CN 12)		CN 2 nd shell at 3.5 Å (theor. CN 6)		CN 3 rd shell at 4.3 Å (theor. CN 24)		CN 7 th shell at 6.6 Å (theor. CN 48)
	PDF	XAS	PDF	XAS	PDF	XAS	PDF
0% H₂/He							
350 °C	-	-	-	-	-	-	-
375 °C	3.5	3.5	0.92	1.6	4.8	3.4	9.8
400 °C	6.9	6.9	3.6	2.4	12.0	7.4	21.4
500 °C	8.1	8.1	3.8	3.8	14.4	17.0	25.2
5 H₂/He							
350 °C	2.7	2.7	1.5	0.3	4.8	2.4	7.4
375 °C	11.8	11.8	5.6	4.2	21.3	24.1	37.9
400 °C	12.0	12.0	5.7	2.1	21.4	12.8	40.7
500 °C	10.5	10.5	5.4	3.6	19.3	19.9	35.3
10 H₂/He							
350 °C	3.5	3.5	1.7	1.9	6.1	2.0	11.2
375 °C	11.3	11.3	5.3	4.5	20.1	15.6	37.0
400 °C	11.5	11.5	5.6	6.4	20.7	17.2	39.6
500 °C	11.4	11.4	5.7	5.1	20.9	21.5	40.4

Note that the CN for 0% H₂/He 350 °C could not be derived, because of a large fraction of Ni(BDC)(PNO) in the sample.

References

- 1 B. Ravel and M. Newville, ATHENA, ARTEMIS, HEPHAESTUS: data analysis for X-ray absorption spectroscopy using IFEFFIT, *J. Synchrotron Radiat.*, 2005, **12**, 537–541. DOI: 10.1107/S0909049505012719.
- 2 T. S. Ertel, H. Bertagnolli, S. Hückmann, U. Kolb and D. Peter, XAFS Spectroscopy of Liquid and Amorphous Systems: Presentation and Verification of a Newly Developed Program Package, *Appl. Spectrosc.*, 1992, **46**, 690–698. DOI: 10.1366/0003702924125069.
- 3 M. Newville, IFEFFIT: interactive XAFS analysis and FEFF fitting, *J. Synchrotron Radiat.*, 2001, **8**, 322–324. DOI: 10.1107/s0909049500016964.
- 4 N. Binsted and S. S. Hasnain, State-of-the-Art Analysis of Whole X-ray Absorption Spectra, *J. Synchrotron Radiat.*, 1996, **3**, 185–196. DOI: 10.1107/S0909049596005651.
- 5 N. Binsted and F. Mosselmans, eds., *EXCURV98 Manual*, Daresbury, UK.
- 6 M. Bauer and H. Bertagnolli, The amplitude reduction factor and the cumulant expansion method: crucial factors in the structural analysis of alkoxide precursors in solution, *J. Phys. Chem. B*, 2007, **111**, 13756–13764. DOI: 10.1021/jp076386i.
- 7 A. Jentys, Estimation of mean size and shape of small metal particles by EXAFS, *Phys. Chem. Chem. Phys.*, 1999, **1**, 4059–4063. DOI: 10.1039/a904654b.
- 8 P. Juhás, T. Davis, C. L. Farrow and S. J. L. Billinge, PDFgetX3 : a rapid and highly automatable program for processing powder diffraction data into total scattering pair distribution functions, *J. Appl. Crystallogr.*, 2013, **46**, 560–566. DOI: 10.1107/S0021889813005190.
- 9 P. Juhás, C. L. Farrow, X. Yang, K. R. Knox and S. J. L. Billinge, Complex modeling: a strategy and software program for combining multiple information sources to solve ill posed structure and nanostructure inverse problems, *Acta Crystallogr., Sect. A: Found. Adv.*, 2015, **71**, 562–568. DOI: 10.1107/S2053273315014473.